remote sensing

MDPI

Article

Long-Term Elevational Redistribution of Vegetation Greenness Along the Dushanzi–Kuqa Transect on the Southern Flank of the Tianshan Mountains

Zekun Ding [1], Xiangzhi Kong [2], Yanhu Mu [1,*], Minghao Liu [1], Zhuang Wang [2], Lingjie Li [1], Lijie Zhang [1] and Wudong Wang [3]

[1] State Key Laboratory of Cryospheric Science and Frozen Soil Engineering, Northwest Institute of Eco-Environment and Resources, Chinese Academy of Sciences, Lanzhou 730000, China
[2] PowerChina Sinohydro Bureau 6 Co., Ltd., Shenyang 110169, China
[3] School of Civil Engineering, Northwest Minzu University, Lanzhou 730030, China
* Correspondence: muyanhu@lzb.ac.cn

Abstract

Mountain vegetation change is commonly summarized as a mean greening or browning trend, or as the displacement of a discrete boundary; both can miss changes in the shape of the elevation profile of vegetation greenness. Here we tested whether the greenness profile on the southern flank of the Tianshan Mountains reorganized between 1989 and 2024, using a Landsat transect along the Dushanzi–Kuqa (G217) highway. NDVI and EVI2 profiles were constructed over a fixed 1000–4100 m elevation domain using only sampling locations valid in all comparison periods; profiles were mean-centered, and the early-to-recent contrast was tested with spatial-block permutations across 36 combinations of temporal window, corridor width, elevation-bin width, and index. All 36 combinations showed significant shape change ($p \leq 0.005$) with cross-scenario concordance, and the contrast persisted after adjustment for cross-sensor differences. The contrast followed a consistent three-band structure, with relative decreases at 1100–1950 m, increases at 2550–3300 m, and renewed decreases at 3550–4100 m. Absolute greenness increased almost everywhere (more than 97% of 25,334 samples), but the increase was four to five times larger in the mid-elevation band than in the lower and upper bands, varied eightfold along the transect, and was organized primarily by elevation and along-transect position (spatially cross-validated random-forest $R^2 \approx 0.66$). The vegetation contrast was not directionally consistent with decadal temperature, soil-moisture, or snow contrasts. Greenness change along this transect was therefore an elevation-dependent redistribution of the whole profile rather than uniform greening or a single boundary displacement, and no robust directional correspondence with decadal hydroclimate contrasts was detected under the present decadal analysis.

Keywords: elevational greenness profile; vegetation redistribution; Landsat time series; NDVI; EVI2; random forest; Tianshan Mountains; spatially matched sampling

Check for updates

Academic Editors: Fei Xiao, Yonghui Yao and Wenzuo Zhou

Received: 1 September 2026
Revised: 19 October 2026
Accepted: 26 October 2026
Published: 29 October 2026

Copyright: © 2026 by the authors. Licensee MDPI, Basel, Switzerland. This article is an open access article distributed under the terms and conditions of the Creative Commons Attribution (CC BY) license.

1. Introduction

Mountain elevational gradients compress a broad spectrum of environmental conditions into short distances and have long served as natural experiments in ecology [1]. Decades of satellite observations have documented widespread changes in mountain vegetation greenness. In most analyses, however, these changes are summarized in one of

two ways, either as a mean trend toward greening or browning or as the displacement of a discrete feature such as a treeline or a vegetation isoline. Both approaches reduce the elevation dimension of the landscape to a scalar or a single displacement estimate. They can therefore miss a structurally distinct mode of change, in which greenness is redistributed among elevation bands—gaining in some and losing in others relative to the profile mean—without a uniform direction or a coherent boundary displacement [2–4].

Evidence that mountain greenness change is organized by elevation has accumulated across mountain systems. In the Himalaya and Hindu Kush, Landsat records document vegetation expansion into subnival zones [5], elevational shifts in alpine greenness with strong longitudinal variation [6], elevation-dependent greening whose climate sensitivity changes sign along the slope [7], and, in the arid western Himalaya, greening trends that temperature, precipitation, and snow metrics cannot explain [8]. In the European Alps, snow-cover loss has been linked to increased high-elevation productivity [9]; in the Andes, forest plot resurveys show widespread but heterogeneous, elevation-structured community responses [10]; and in an arid Central Asian mountain–basin system, the sign of the greenness–climate relationship reverses along elevation [11]. Regionally aggregated greening can further conceal simultaneous browning that varies through time [12]. Across these remote-sensing studies, change is primarily summarized as band-specific trends, greening magnitudes, vegetation expansion, or boundary displacements, leaving the shape of the whole greenness profile untested.

Discrete boundaries are a particularly demanding target for long-term change detection. Ecotones are rarely sharp lines; they typically occupy zones of mixed composition and gradual turnover, so their mapped position is sensitive to classification uncertainty [13]. In remote-sensing analysis, an estimated boundary is not only an ecological feature but also a statistical construct shaped by spatial scale, measurement type, spatial support, and the detection method [14,15]. Detection uncertainty is greatest where transitions are gradual, local contrast is weak, or moderate-resolution pixels integrate heterogeneous vegetation structure [15,16]. Multi-indicator agreement can narrow a transition range, as shown for the Bogda Mountains within the Tianshan [17], but each indicator-specific boundary remains estimator-dependent. Treeline research has accordingly shifted from tracking boundary displacement alone toward multidimensional descriptions of ecotone width, structure, and dynamics [18]. A profile-level analysis follows the same logic and evaluates the elevation–greenness relationship as a whole, without requiring that a discrete boundary be stable, uniquely defined, or ecologically labeled a priori.

The Tianshan Mountains of Central Asia provide a stringent setting for such an analysis, because vegetation change along their elevational gradients is spatially heterogeneous and strongly constrained by an arid continental climate. Landsat-based reconstructions show that individual altitudinal vegetation belts and subregions did not respond uniformly during 1989–2015 [19]. Regional NDVI analyses indicate that the apparent greening was temporally nonstationary, with a post-1998 reversal toward browning in parts of the range under increasing soil-water limitation [20], consistent with the broader Central Asian evidence that vegetation growth is increasingly water-limited [21] and that greening–browning trend direction and drought sensitivity shift with the analysis period [22,23], and MODIS-era records show elevation-dependent but spatially variable shifts in green-up dates [24]. A single displacement metric is unlikely to capture change of this kind. A fixed-support profile analysis, by contrast, can test whether the elevational organization of vegetation greenness has changed without presupposing a particular boundary movement or mechanism.

Applying this framework to the Landsat archive requires more than the bitemporal comparisons that historically dominated change detection [25,26]. Apparent profile change can arise from observation artifacts, including changing data availability across

elevations, period-specific cloud and cloud-shadow masking, and mismatched elevation domains [27,28]; alpine greening trends, in particular, are inflated where the density of summer observations increases over time [28]. Landsat change estimates also depend on index choice, preprocessing, and algorithmic decisions [26,29]. Canopy structural complexity can further decouple index-based greenness from vegetation function [30], and the expanding family of index formulations—soil-adjusted, nonlinear-kernel, and near-infrared-reflectance variants [31–34]—makes reliance on any single index increasingly difficult to defend. A rigorous test must therefore (i) hold the sampled population and the elevation domain constant across periods, (ii) separate profile-shape change from uniform mean greenness change, and (iii) remain stable across plausible alternative temporal, spatial, binning, and index specifications. This combination of spatially matched sampling, shape-focused testing, and cross-specification confirmation has rarely been applied to elevational vegetation change in arid mountain systems. For the Tianshan specifically, elevation-resolved analyses have addressed altitudinal belt positions [19], regional greenness trends [20], and green-up timing [24]. To our knowledge, however, neither long-term change in the shape of the whole elevation–greenness profile under these controls nor its directional correspondence with decadal hydroclimate contrasts has been tested.

Detection alone, however, does not determine interpretation. A corridor-wide profile contrast can conceal strong heterogeneity along the transect, so the spatial distribution of the contrast—and its organization by terrain structure other than elevation, such as slope and aspect—must be established before the profile pattern can be interpreted. Independently, an elevation-dependent greenness change in a water-limited mountain system invites a hydroclimatic explanation, but that explanation should be tested rather than assumed, for example by evaluating whether the vegetation contrast is directionally consistent with decadal contrasts in temperature, soil moisture, and snow conditions. Treating detection, spatial organization, and environmental consistency as separate, sequentially ordered questions ensures that attribution is addressed only after detection and characterization.

Here we address all three questions in sequence along the Dushanzi–Kuqa (G217) highway, which crosses the Chinese Tianshan from the northern to the southern piedmont, using Landsat observations from 1989 to 2024 and focusing on the southern flank of the range. The sequence reflects a logical dependency: a profile-shape change must first be shown to be real under controls for observation artifacts; only then is it meaningful to characterize where the change occurred and how it is organized by terrain; and only with the phenomenon and its spatial extent fixed should environmental consistency be tested, so that attribution is not attempted on an artifact or on a spatially ambiguous signal. The highway serves only to define a continuous, reproducible geographic sampling line; it is not treated as an exposure, and no road-distance variable enters the analysis. We (1) test whether the elevation profile of vegetation greenness (NDVI and EVI2; hereafter the greenness profile) on the southern flank reorganized between early and recent Landsat periods, using outcome-blind spatially matched sampling, mean-centered profiles, spatial-block permutation tests, and an intersection rule across 36 specification combinations; (2) quantify where the change occurred and how strongly it is organized by terrain structure, combining sample-level change maps and along-transect summaries with a spatially cross-validated random-forest analysis; and (3) test whether the vegetation contrast is directionally consistent with decadal hydroclimate contrasts under a separately frozen design.

2. Study Area, Dataset and Methods

2.1. Study Area

The study was conducted along a Landsat transect following the Dushanzi–Kuqa (G217) highway across the Chinese Tianshan (Figure 1). The route extends from the northern

piedmont near Dushanzi to the southern piedmont near Kuqa (approximately 526 km) and crosses one of the strongest topographic gradients in the range. The distance along the route allowed the transect to be divided a priori into geomorphically interpretable segments while keeping the sampling frame fixed across all Landsat periods.

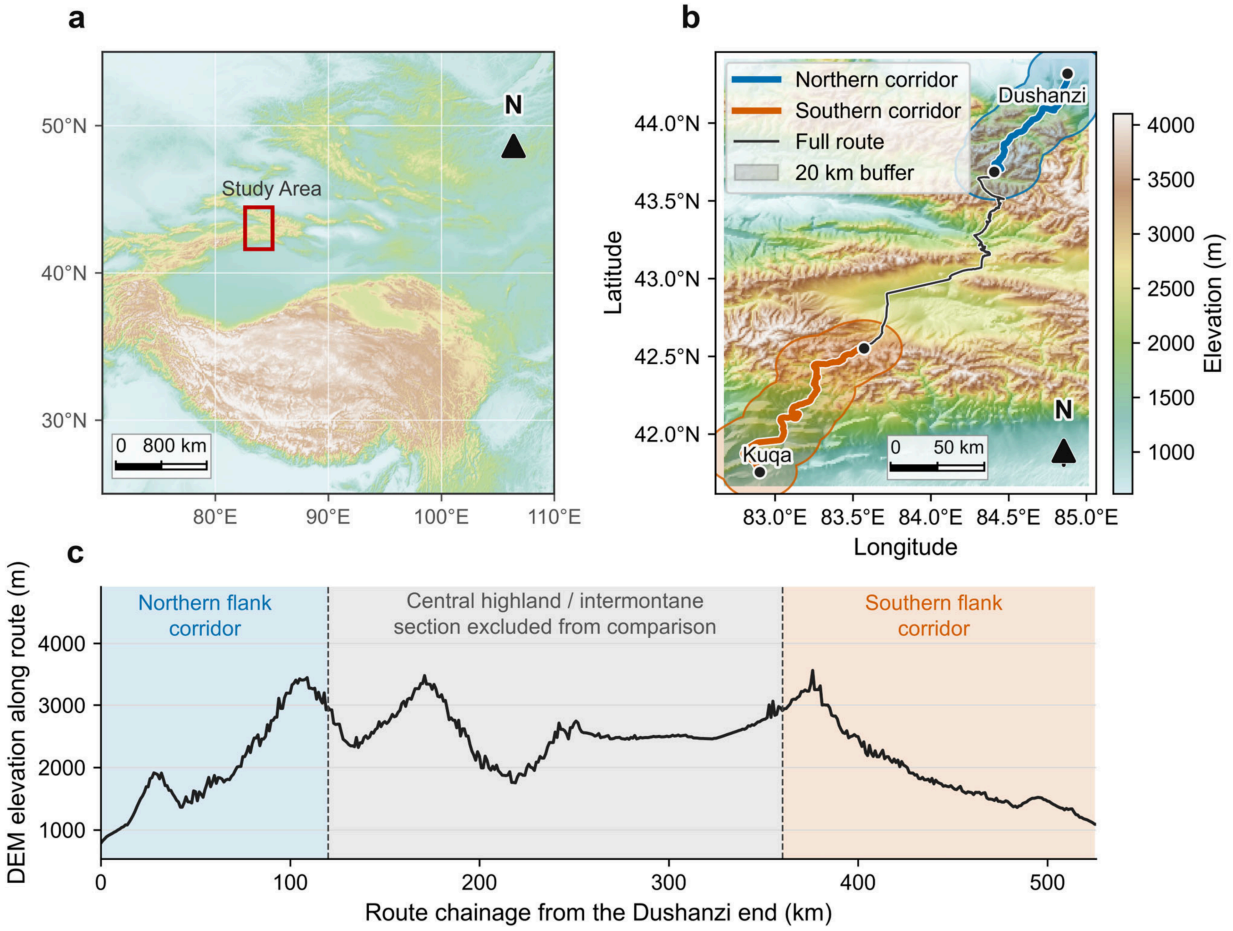


Figure 1. Study region, sampling transects, and elevational framework across the Tianshan Mountains. (**a**) Macro-location of the Dushanzi–Kuqa transect. (**b**) The Dushanzi–Kuqa route on a DEM hillshade, with 20 km corridor buffers. (**c**) DEM elevation profile along the route.

Two terminal corridors were retained for analysis. The northern corridor (0–120 km route distance) and the southern corridor (360–525 km) each form a relatively coherent flank-scale elevational gradient. The intervening central high-mountain and intermontane section was excluded from primary inference because it mixes ridge, valley, and basin settings and does not form a single north- or south-facing elevational profile. The corridors were delineated by route distance rather than by pixel-level terrain aspect, so each contains a mixture of local slope aspects; the aspect-stratified analysis in Section 2.6 tests whether the profile structure is sensitive to this mixture. Corridor width was treated as a design parameter rather than as an ecological distance from the road. The 20 km corridor served as the primary width, and the 10 and 30 km corridors were retained for spatial-scope sensitivity. The southern corridor is the primary inference region; the northern corridor serves only as a comparator and quality-control context, and no south-versus-north asymmetry claim is made.

2.2. Landsat Data and Temporal Compositing

Surface reflectance observations were obtained from the Landsat Collection 2 Tier 1 Level-2 archive (TM, ETM+, OLI, and OLI-2) [25,35]. Landsat MSS was excluded to

avoid mixing spatial and spectral regimes. All imagery was restricted to the growing season (1 June–30 September), and invalid observations were removed using the Collection 2 quality-assessment bands (fill, dilated cloud, cirrus, cloud, and cloud shadow) and radiometric-saturation flags before compositing [35]; snow- and water-flagged observations were retained and are addressed in the Limitations. Within each period, annual growing-season medians were first computed, and a single representative annual composite was then selected by a cross-year medoid rule over the analytical bands: for each pixel, the spectral center of the period was defined as the across-year median of the annual medians over the reflective bands, and the annual composite closest to that center was selected, so the representative year can vary from pixel to pixel rather than being fixed scene-wide. The medoid was preferred over a direct multi-year median because it retains the within-year phenological coherence of an actually observed year and is less sensitive to outlier years; a robustness comparison against the multi-year median is reported in the Supplementary Materials. Two greenness indices were used. NDVI served as the standard long-term index [36], and EVI2 provided an independent formulation derived from the red and near-infrared bands alone [37]; the main inference was required to hold for both.

$NDVI$ served as the standard long-term index, with a continuous Landsat interpretation spanning the TM to OLI-2 era [36]:

$$NDVI = \frac{\rho_{NIR} - \rho_{Red}}{\rho_{NIR} + \rho_{Red}} \quad (1)$$

where ρ_{NIR} and ρ_{Red} denote the masked surface reflectances in the near-infrared and red bands, respectively. EVI2 provides an independent formulation derived from the red and near-infrared bands alone; by omitting the blue band and adjusting for canopy background, it reduces soil-brightness and aerosol influences while remaining computable identically across all four sensors [37]:

$$EVI2 = 2.5 \times \frac{\rho_{NIR} - \rho_{Red}}{\rho_{NIR} + 2.4\rho_{Red} + 1} \quad (2)$$

where ρ_{NIR} and ρ_{Red} are as defined in Equation (1). The $EVI2$ coefficients are the fixed global calibration of Jiang et al. [37], designed for sparse-to-moderate canopies and for identical computation across sensors. No local recalibration was attempted: no field spectra exist for this transect, and requiring the inference to hold across structurally different indices—extended to kNDVI [33], the soil-adjusted SAVI [31] and MSAVI [32], and the water-sensitive NDMI [38] in the Supplementary Materials—bounds index-formulation effects empirically rather than by assumption. The main inference was therefore required to hold for both indices, so that index-specific formulation or saturation behavior cannot by itself account for a confirmed profile contrast.

Two temporal-window designs were implemented. The six-year design used early, middle, and recent periods of 1989–1994, 2003–2008, and 2019–2024, and the ten-year design used equal-length periods of 1989–1998, 2002–2011, and 2015–2024. The ten-year windows serve as the primary compositing design because they improve early-period high-elevation observation support while preserving equal window length; the six-year windows test sensitivity to this choice. Pixels with fewer than three valid growing-season observations accumulated within a period remained masked and were not gap-filled (Figures 2 and 3).

2.3. Spatially Matched Sampling and Elevation Domains

All spatial analyses were conducted in UTM Zone 45N (EPSG:32645). A fixed 500 m sampling grid was generated once and applied across all temporal-window designs, corridor widths, regions, and periods. Elevation, slope, northness, and eastness at the grid

centers were derived from a single Copernicus DEM GLO-30 reference in the same projection [39], so that spatial locations and terrain assignments were identical among periods.

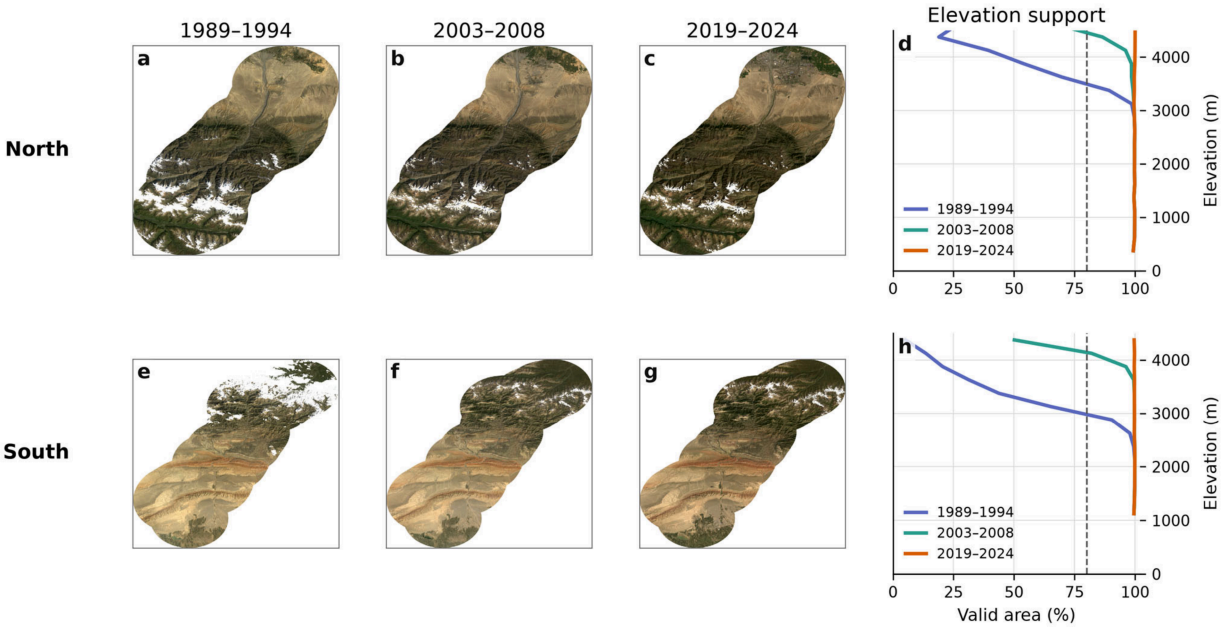


Figure 2. Six-year composite quality control. (**a**–**c**) RGB composites for the northern corridor for 1989–1994, 2003–2008, and 2019–2024, respectively; (**d**) elevation-stratified valid-area curves for the northern corridor; (**e**–**g**) RGB composites for the southern corridor for the same periods, respectively; (**h**) elevation-stratified valid-area curves for the southern corridor.

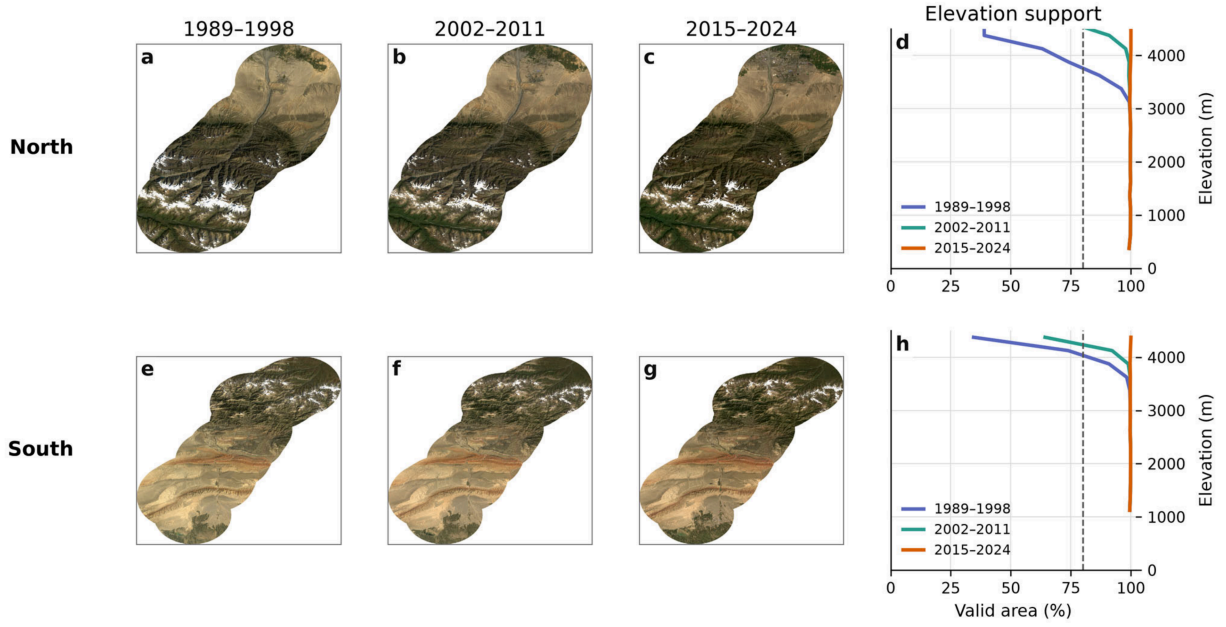


Figure 3. Ten-year composite quality control. (**a**–**c**) RGB composites for the northern corridor for 1989–1998, 2002–2011, and 2015–2024, respectively; (**d**) elevation-stratified valid-area curves for the northern corridor; (**e**–**g**) RGB composites for the southern corridor for the same periods, respectively; (**h**) elevation-stratified valid-area curves for the southern corridor.

For each combination of temporal-window design, corridor width, and region, only grid-center locations with valid composite data in all three periods were retained, with validity determined from the period-specific quality and observation-count masks before

index extraction. NDVI and EVI2 were then computed at each retained location from the masked red and near-infrared reflectances of the 30 m composites (Equations (1) and (2)). This three-period matched sample set—used unchanged for the early, middle, and recent profiles—ensures that temporal contrasts cannot arise from changes in the sampled locations. Under the primary ten-year, 20 km design, it contained 25,334 locations in 295 five-kilometer blocks in the south and 18,916 locations in 224 blocks in the north.

The matched samples were grouped into elevation bins using the fixed DEM elevations, with a 50 m bin width in the primary analysis and 30 and 100 m widths for sensitivity tests. A bin was retained only if it contained at least 10 matched samples distributed across at least three 5 km spatial blocks under every temporal-window and corridor-width setting, yielding 63 bin centers from 1000 to 4100 m in the southern corridor and 75 from 500 to 4200 m in the northern corridor; the reported elevation limits therefore refer to bin centers, not bin edges. Within each retained bin, mean greenness was calculated separately by period, index, region, temporal-window design, and corridor width. The resulting profiles represent elevation-conditioned greenness and provide the observational basis for the profile-shape analysis; they should not be interpreted as classified vegetation belts, discrete vegetation-boundary locations, or changes in total vegetated area.

2.4. Mean-Centered Profile-Shape Testing

For each scenario, region, index, and bin width, the elevational greenness profile g(z) was defined as the median greenness within each accepted elevation bin z. To separate profile-shape change from a uniform change in mean greenness, each profile was centered on its own mean across the fixed elevation domain:

$$g_c(z) = g(z) - \overline{g} \tag{3}$$

where $\overline{g}$ is the mean of g(z) across all accepted bins. The early-to-recent centered contrast is

$$D(z) = g_{c,\text{recent}}(z) - g_{c,\text{early}}(z) \tag{4}$$

D(z) describes how the relative distribution of greenness across elevation changed between periods, not whether the profile as a whole became greener or browner. Figure 4 illustrates this profile-shape description against whole-profile mean greening and boundary displacement. The middle period is retained for visual and temporal context but does not enter the primary test. The magnitude of shape change was summarized by an L2 norm across bins:

$$T_{L2} = \sqrt{\sum_z D(z)^2 \, \Delta z} \tag{5}$$

where Δz is the constant bin width; magnitudes are compared only within a common bin width. Null distributions were generated by swapping early and recent period labels at the 5 km block level (4999 permutations per test); a contrast was supported at $p < 0.05$ and is reported as $p < 0.001$ when no permutation exceeded the observed value. A uniform whole-profile greenness increase, removed by centering, cannot by itself produce a significant result.

Confirmation required both statistical significance and cross-parameter consistency. For each scenario, bootstrap-centered contrasts were compared, using cosine similarity, with the mean consensus contrast of the other five scenarios sharing the same bin width and index (i.e., the other temporal-window and corridor-width combinations), over 1999 shared Poisson spatial-block bootstrap replicates. Concordance required a positive 2.5th-percentile bound and a valid-replicate fraction above 0.90. For the southern corridor, confirmation required all 36 combinations to pass both criteria, so that no isolated positive test can establish the inference.

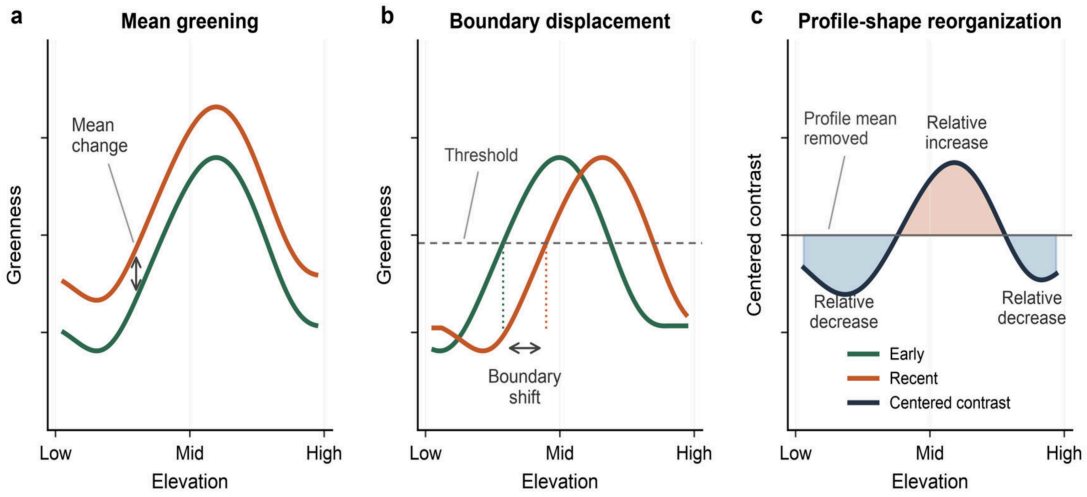


Figure 4. Three descriptions of mountain greenness change. (**a**) Mean greening; (**b**) boundary displacement; (**c**) profile-shape reorganization, quantified by D(z). Green and orange denote early and recent profiles. In (**b**), dashed and dotted lines show the threshold and boundary positions; in (**c**), the dark curve is D(z), the zero line is the removed profile mean, and blue/orange shading denotes relative decreases/increases.

2.5. Cross-Sensor Falsification Check

To evaluate whether the Landsat sensor chain could account for the early-to-recent contrast, a bridge test was conducted on the primary southern corridor and the frozen 1000–4100 m, 50 m-bin domain. The sensor-related component of the profile contrast was estimated from overlapping TM–ETM+ (1999–2011) and ETM+–OLI (2013–2021) records, with bridge–elevation support groups held to the same frozen support criteria (126 of 126 eligible). The estimated sensor contrast was projected onto the observed early-to-recent contrast (projection fraction, with 95% spatial-block bootstrap intervals), and the sensor-adjusted contrast—observed minus estimated—was compared with the observed contrast using cosine similarity. The sensor chain is judged unable to account for the reorganization if the projection fraction is well below unity and the adjusted contrast retains the observed structure.

2.6. Spatial-Pattern and Terrain-Association Analysis

To establish where the change occurred and how it is organized by terrain, sample-level early-to-recent differences (ΔNDVI, ΔEVI2) were analyzed on the primary southern design. Three complementary summaries were used. First, maps of the absolute sample-level differences over the corridor were produced, with elevation contours marking the main contributing bands identified in Section 3.2. Second, along-transect summaries were computed by assigning samples to the nearest route chainage and aggregating them into 10 km segments with 95% spatial-block bootstrap intervals. Third, 5 km block-level statistics were derived, including the fraction of blocks with positive mean change, the contribution concentration across blocks, and a within-block centered L2 statistic quantifying the pervasiveness of profile reorganization inside individual blocks. Because the sample-level differences are not centered, these summaries describe absolute change; the centered-profile inference remains that of Section 2.4.

The maps and stratified contrasts describe where the change occurred, but they cannot quantify how strongly the change is organized by terrain, nor separate the contributions of correlated terrain attributes. These two questions require a multivariate model, evaluated out of sample. Terrain association was therefore evaluated two ways. First, stratified profile contrasts were computed within aspect (northness ≥ 0 versus <0) and slope (<15°, 15–25°,

>25°) strata to test whether the three-band contrast structure is stable across terrain classes. Second, a random-forest regressor (500 trees, minimum leaf size 5, fixed random seed; code available as noted under Data Availability) was fit with ΔNDVI (and ΔEVI2) as the response and elevation, slope, northness, eastness, and route chainage as predictors. Model performance was evaluated with spatial cross-validation over 5 km blocks (ten folds), and predictor importance was quantified by permutation importance computed on held-out blocks; partial dependence was used to inspect the functional form of the leading predictors. This analysis describes the terrain organization of the observed change; it does not identify climatic or ecological drivers, and no road-related predictor was included.

2.7. Decadal Hydroclimate Consistency Test

A separately frozen design was used to test whether the confirmed vegetation contrast is directionally consistent with decadal hydroclimate contrasts. For the same scenarios and spatially matched sampling locations, decadal (and, for sensitivity, six-year) contrasts of ERA5-Land monthly aggregates were computed for near-surface air temperature, volumetric soil water, and snow water equivalent (SWE), hereafter the energy, water, and snow groups, at the native ERA5-Land grid, paired with the vegetation samples by elevation bin. ERA5-Land values (~0.1° cells) were not lapse-rate adjusted to sample elevations, so within-cell elevation structure is smoothed; this is conservative for detecting spurious elevation-aligned associations, because cell-scale climate values cannot generate fine-scale elevational structure in $D_{clim(z)}$. Directional consistency between the vegetation contrast $D_{veg(z)}$ and each climate contrast $D_{clim(z)}$ was quantified by a signed inner product (IP) and a Spearman rank correlation (ρ), with paired spatial-block bootstrap replicates and block sign-flip permutations. The design admits only two conclusions—"directionally consistent" or "no association"—and explicitly excludes attribution and process ranking. Because $D_{veg(z)}$ is mean-centered, the inner product is orthogonal by construction to any climate contrast that is uniform across elevation; the test therefore has power only against elevation-structured climate signals aligned with the vegetation contrast, and a spatially uniform forcing cannot be detected as consistent even if it contributed to the change. CHIRPS precipitation aggregates (May–August and November–May, corresponding to the growing-season moisture and cold-season snow periods) were evaluated as an independent moisture-proxy sensitivity check and are reported alongside the ERA5-Land soil-water result. The northern corridor was analyzed with the same contrast design for exploratory context, but without centering, so the northern statistics are not comparable in kind with the centered southern test.

3. Results

3.1. Southern Greenness Profiles Reorganized Between Early and Recent Periods

The southern corridor showed a clear early-to-recent change in the relative distribution of greenness across elevation (Figure 5). In the primary design (10-year windows, 20 km corridor, 50 m bins), both NDVI and EVI2 profiles changed shape after centering, so the recent profile is not simply a vertically shifted version of the early one. The whole-profile L2 statistic was 2.92 for NDVI and 1.82 for EVI2 (both $p < 0.001$). Mean greenness increased over the same period contrast (+0.070 in NDVI and +0.040 in EVI2 units, an equal-weighted mean across elevation bins; the area-weighted sample mean reported in Section 3.3 is +0.065—the two estimators weight elevation differently and need not coincide), but because each profile was centered before differencing, this uniform increase cannot by itself generate the shape contrast. The same direction of contrast appeared in both indices, and all 36 specification combinations passed both the permutation test and the concordance criterion (Section 3.5), so the reorganization is stable across temporal-window,

corridor-width, bin-width, and index choices. The middle period (2002–2011), which does not enter the primary test, is consistent with a gradual progression rather than a step change: its centered profile falls between the early and recent profiles in 54 of 63 bins for NDVI and 57 of 63 for EVI2, and the early-to-middle and early-to-recent centered contrasts correlate at r = 0.94–0.97 (Figure 6).

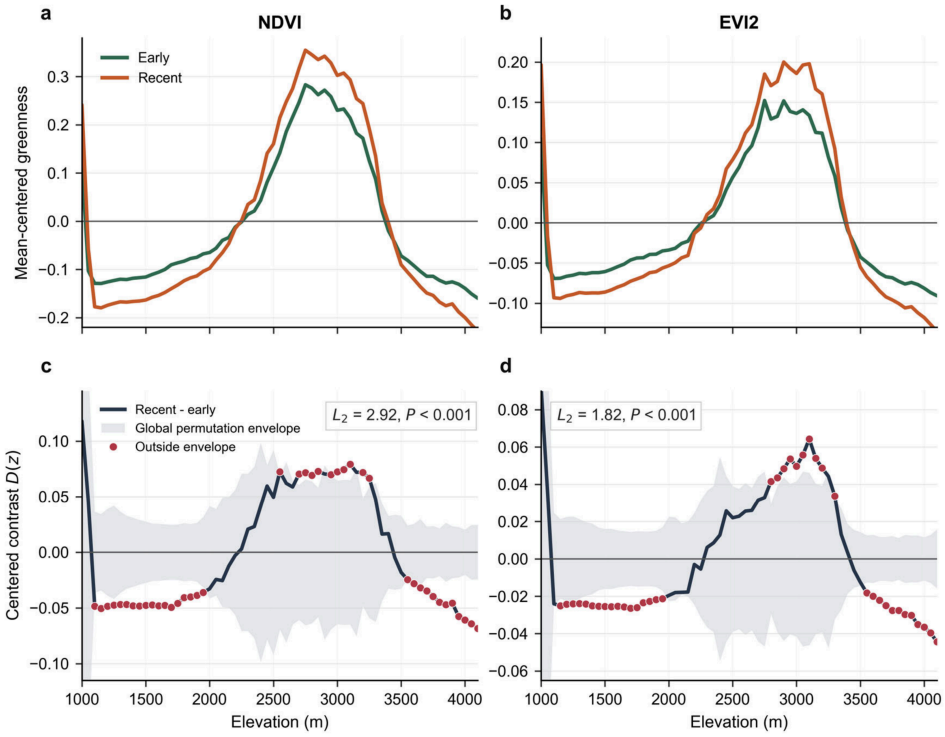


Figure 5. Early-to-recent reorganization of the southern greenness profile in the primary design (10-year windows, 20 km corridor, 50 m bins). (**a**,**b**) Mean-centered NDVI and EVI2 profiles for the early (1989–1998) and recent (2015–2024) periods. (**c**,**d**) Centered contrasts D(z) with the simultaneous global permutation envelope (gray band, 4999 spatial-block permutations); red dots mark bins whose contrast falls outside the simultaneous envelope.

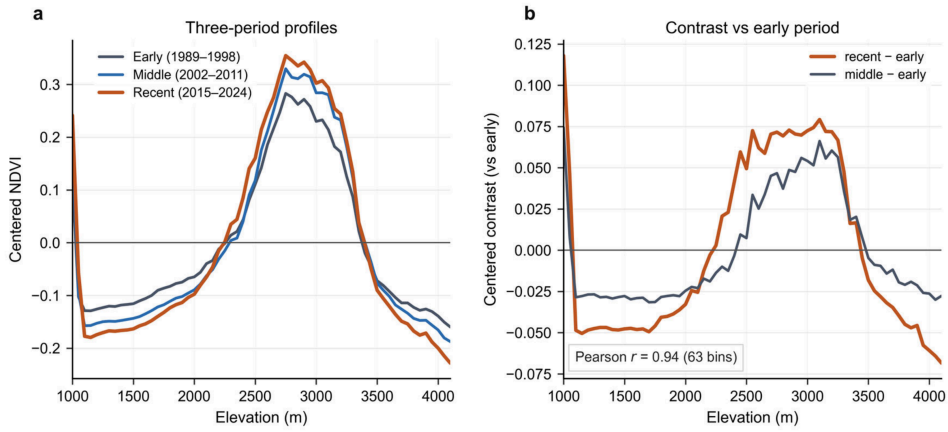


Figure 6. Temporal progression of the southern greenness-profile reorganization (NDVI, primary design). (**a**) Mean-centered profiles for the early (1989–1998), middle (2002–2011), and recent (2015–2024) periods; the middle profile falls between the early and recent profiles in 54 of 63 elevation bins. (**b**) Early-to-middle and early-to-recent centered contrasts; the two correlate at r = 0.94, indicating a gradual progression of the reorganization rather than a recent step change. EVI2 shows the same behavior (57 of 63 bins, r = 0.97; Figure S1).

3.2. A Consistent Three-Band Elevational Structure

The reorganization was concentrated in specific elevation bands rather than spread uniformly across the 1000–4100 m domain (Figure 5c,d). For NDVI, bins outside the permutation envelope were concentrated at 1100–1950 m and 3550–4100 m for negative contrasts, with positive departures occurring discontinuously between 2550 and 3250 m; EVI2 showed the same structure, with negative departures at 1150–1950 m and 3550–4100 m and positive departures between 2800 and 3300 m. Because profiles were centered, these signs describe relative redistribution within the domain, not absolute gain or loss (Section 3.3 quantifies the absolute changes). Contributions were concentrated in the mid-elevation band, which alone accounted for 45.0% (NDVI) and 46.8% (EVI2) of the squared L2 magnitude, yet the result was not numerically dominated by any single bin or by the domain edges: no single 50 m bin contributed more than 17.9% of the squared L2 magnitude, and the two domain-edge bins together contributed at most 20.1%. The largest single-bin contribution occurred at the lowest bin (1000 m), which includes part of the oasis cropland and lies outside all three bands, so it cannot generate the three-band structure.

3.3. Pervasive Greening with Strong Mid-Elevation Amplification Across the Corridor

The absolute sample-level changes place the centered contrast in physical terms (Figure 7). Greenness increased almost everywhere: 97.7% of the 25,334 southern samples gained NDVI between the early and recent periods (area-weighted sample mean ΔNDVI = +0.065, ΔEVI2 = +0.040, an estimator weighted by sampled area, distinct from the equal-weighted bin mean of +0.070 in Section 3.1), and 292 of 295 five-kilometer blocks (99.0%) had positive block means, with the top-contributing 20% of blocks accounting for only 46–48% of the total change. The increase was therefore pervasive rather than driven by a few locations.

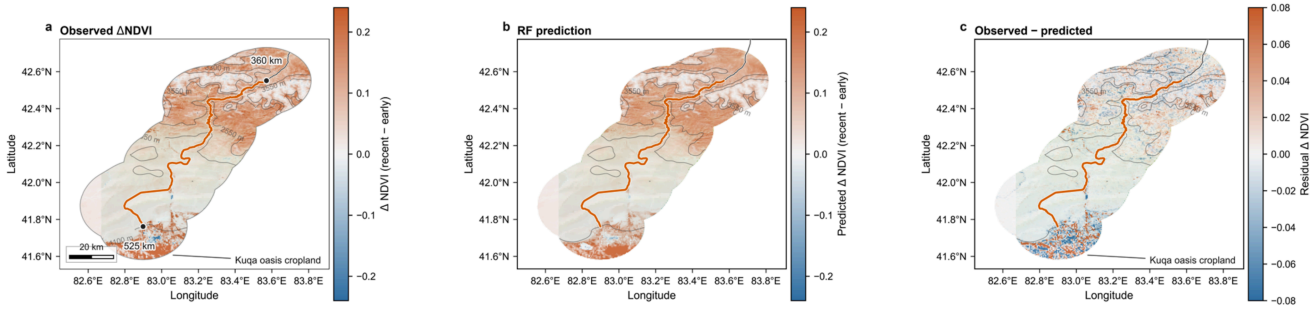


Figure 7. Spatial distribution of the absolute early-to-recent change in greenness across the southern corridor (primary design, not mean-centered). (**a**) Observed ΔNDVI per 500 m sample, gridded over a DEM hillshade, with elevation contours marking the main contributing bands (1100–1950 m, 2550–3300 m, 3550–4100 m) and the route overlaid; the Kuqa oasis cropland hotspot is annotated, and saturated cells within it are localized cropland-loss pixels reaching the color-scale limit, not plotting artifacts. (**b**) Random-forest-predicted ΔNDVI on the same color scale as (**a**). (**c**) Observed-minus-predicted residuals; residuals are small across the corridor but large and sign-mixed within the Kuqa oasis cropland (annotated), where the change is not terrain-organized. The ΔEVI2 map is visually similar (Figure S1).

Its magnitude, however, was strongly structured. The mid-elevation band (2550–3300 m) gained +0.127 in mean NDVI, four to five times the gains of the lower (1100–1950 m, +0.027) and upper (3550–4100 m, +0.030) bands—the same three-band organization identified by the centered test (Section 3.2), now expressed as differential amplification of an almost universal increase. Measured against early-period baselines (band-mean NDVI 0.378, 0.059, and 0.043 for the mid, lower, and upper bands; EVI2 0.220, 0.039, and 0.024), these gains

correspond to increases of roughly 34–37% in the mid-elevation band versus 42–46% and 56–70% in the lower and upper bands: the mid-elevation band dominates the absolute gain, while the largest percentage increases occur where baseline greenness is lowest. Along the transect, 10 km segment medians of ΔNDVI varied eightfold (0.017–0.139), with 18 of 20 segment intervals excluding the corridor-wide median (Figure 8a); the strongest increases coincided with the mid-elevation slopes of the northern part of the southern corridor, and profile reorganization was also pervasive within blocks (median within-block centered L2 = 0.60 for NDVI). A distinct secondary increase occurred at the southern corridor terminus (520–530 km, approximately 1100 m), corresponding to the Kuqa oasis cropland (Figure 7a); this low-elevation agricultural signal is treated separately from the mountain signal below. A masking experiment using ESA WorldCover 2021 [40] quantifies this separation: cropland-labeled samples make up 1.0% of the lower-band (1100–1950 m) samples and account for only 6.9% (NDVI) and 9.1% (EVI2) of the lower-band contrast energy, and excluding them leaves the lower-band relative decline unchanged in sign in all 18 bins (Supplementary Section S7). The lower-band relative decline is therefore a property of the natural and semi-natural vegetation rather than of cropland expansion, abandonment, or irrigation change. Because WorldCover is a single-epoch (2021) product, this experiment excludes present-day cropland but cannot resolve two-date cropland dynamics; a period-paired mask from an annual land-cover record [41] would be needed for that separation.

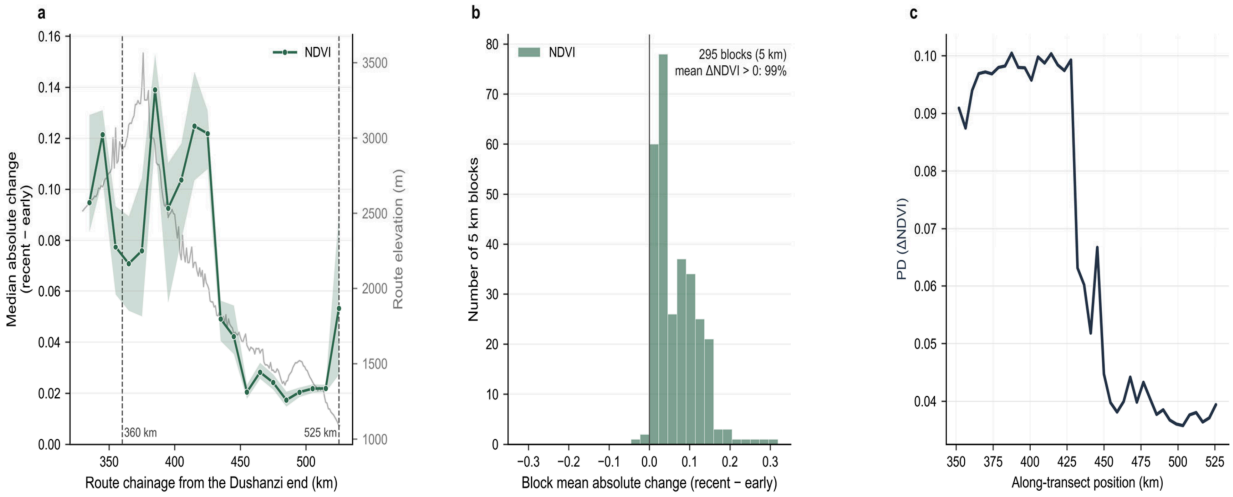


Figure 8. Spatial robustness and along-transect organization of the southern change (NDVI; EVI2 results were similar). (**a**) Median absolute ΔNDVI per 10 km along-transect segment, with 95% spatial-block bootstrap intervals; the gray line shows route elevation (right axis), and dashed lines mark the nominal corridor extent (360–525 km); segments are defined by nearest route chainage and can extend slightly beyond the nominal endpoints. (**b**) Distribution of 5 km block-mean ΔNDVI; 292 of 295 blocks (99%) are positive for both ΔNDVI and ΔEVI2. (**c**) Random-forest partial dependence of ΔNDVI on along-transect position, showing the step-like transition near chainage 430 km discussed in Section 3.4.

3.4. Terrain Association of the Change

The three-band structure was stable across terrain classes (Figure 9). Within every aspect and slope stratum with data, the sign of the stratified centered contrast matched the full-sample structure in both indices (Spearman correlation with the full-sample profile 0.912–0.988); terrain classes modulated the amplitude and peak position of the contrast but not its organization. The only exception was the gentle-slope stratum (<15°), which contains no samples above approximately 3550 m and therefore cannot inform the upper band.

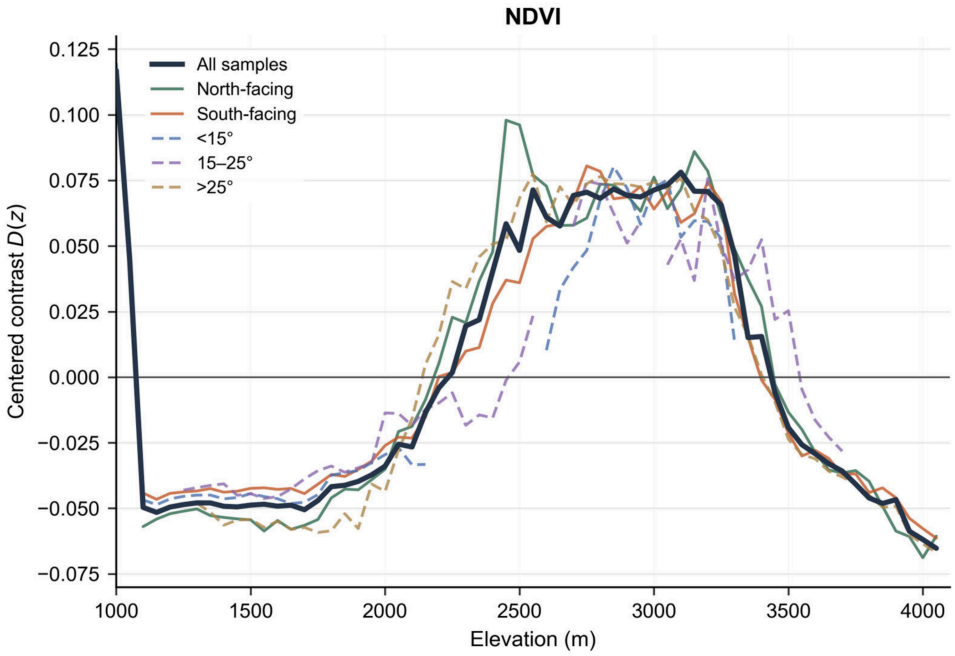


Figure 9. Robustness of the three-band structure across terrain classes (NDVI, primary design). Stratified centered contrasts (thin lines: two aspect and three slope strata) with the full-sample contrast (bold). The three-band structure is retained across all strata with data; the gentle-slope stratum (<15°) has no samples above ~3550 m and therefore cannot inform the upper band. Strata contrasts are centered over their own stratified sample support.

A spatially cross-validated random forest quantified how much of the change is organized by terrain (Figure 10). The model explained about two-thirds of the out-of-sample spatial variance in ΔNDVI and ΔEVI2 (held-out-block R^2 = 0.656 and 0.653; in-sample R^2 = 0.87), so most of the change is predictable from terrain structure alone, whereas about one-third is not. Because elevation and route chainage are strongly collinear along the corridor, predictor importance was quantified with collinearity-aware permutation analyses. Permuting the elevation–chainage pair jointly reduced held-out-block performance by 1.09 (ΔNDVI) and 1.13 (ΔEVI2) R^2 units, far more than permuting the remaining terrain attributes jointly (0.24 and 0.20; individually: slope 0.220 and 0.208, northness 0.129 and 0.085, eastness negligible), so the position–elevation gradient dominates the terrain organization of the change. The joint importance is smaller than the sum of the two single-variable importances (elevation 0.78 and 0.85; chainage 0.60 and 0.38), indicating partial substitution under collinearity. Conditional permutation within five quantile strata of the other predictor attributes most of the pair's importance to elevation: elevation retained 0.57 (ΔNDVI) and 0.63 (ΔEVI2) within chainage strata, whereas chainage retained only about 0.10 within elevation strata. The elevation association is therefore not an artifact of the shared spatial trend, and along-transect position adds little beyond elevation (joint and conditional importance tables in the Supplementary Materials). Partial dependence reproduced the three-band elevational form (Figure 10b) and a step-like transition near chainage 430 km (Figure 8c). This transition coincides with the steepest route-elevation drop of the southern corridor (segment means 2613 m upstream versus 1491 m downstream), and early-period observation counts show no step across it (segment means 12.1 versus 12.7 valid observations), so it is not a Landsat scene-footprint artifact but a transition collinear with the elevation decline. Because elevation and chainage are strongly collinear along the corridor, these two predictors are interpreted jointly as a position–elevation gradient rather than as independent effects. The model residuals isolate change that terrain structure does not organize. They were small across most of the corridor (median ≈ 0; 5th–95th percentile −0.03

to +0.03) but large and sign-mixed within the Kuqa oasis cropland (Figure 7c), confirming that the low-elevation agricultural change is not organized by terrain in the same way as the mountain signal.

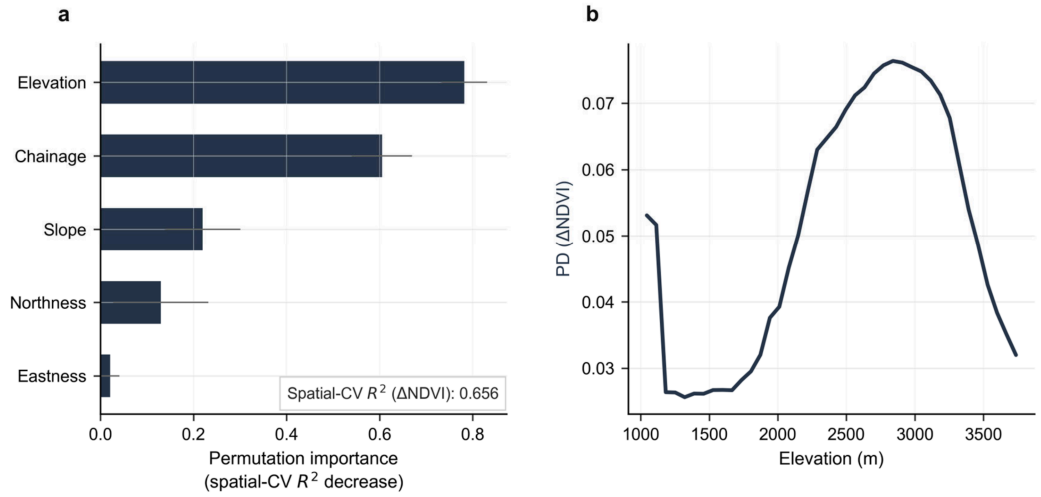


Figure 10. Random-forest association of the change with terrain structure (ΔNDVI). (**a**) Permutation importance under 5 km block spatial cross-validation (held-out R^2 annotated). (**b**) Partial dependence on elevation; the partial dependence on along-transect position is shown in Figure 8c. Elevation and chainage are strongly collinear and are interpreted jointly.

3.5. Robustness Across Specifications and the Sensor Chain

The reorganization was not specific to the primary parameter setting. All 36 southern L2 permutation tests passed—30 of 36 with $p < 0.001$ and the remainder with $p \leq 0.005$—with T_{L2} ranging from 2.67 to 3.20 for NDVI and from 1.55 to 1.98 for EVI2. All 36 concordance checks also passed (median cosine similarity 0.90–0.98; lower bootstrap bounds 0.68–0.95; valid-replicate fraction ≥ 0.987). Consistent with this concordance, the six scenario-level contrasts retained the same three-band organization across both temporal-window designs and all three corridor widths. In the northern comparator, 29 of 36 tests passed, with all failures confined to the 10 km corridor; the northern result is therefore used only for quality-control context. Four further spectral indices recovered the same three-band structure: kNDVI [33] (a nonlinear NDVI variant, tanh of squared NDVI; L2 = 2.81, cosine 0.95 with the frozen NDVI contrast) and the water-sensitive NDMI [38] (L2 = 1.79), both computed on the full matched support, and the soil-adjusted SAVI and MSAVI [31,32] (L2 = 1.73 and 1.74, respectively; cosine ≥ 0.97 with the frozen NDVI contrast) (all $p < 0.001$), so the reorganization is not specific to the NDVI/EVI2 pair (multi-index details in the Supplementary Materials). Likewise, raising the early-period minimum valid-observation threshold from 3 to 5, 8, or 10 left the three-band structure, the upper-band relative decline, and the significance intact (L2 = 2.70–2.89 for NDVI and 1.66–1.80 for EVI2; $p < 0.001$ throughout; cosine ≥ 0.98 with the frozen contrast), although thresholds of 8 and above remove the highest elevation bins from support (Section 2.3 rules; Table S1, Figure S2). Three further checks addressed the temporal observation imbalance directly. Recompositing the recent period with per-year scene counts thinned to the early-period density (median 4.0 valid observations, below the early-period median of 13.6) retained the three-band structure (L2 = 2.76 and 1.83; $p < 0.001$; cosine 0.91 and 0.93 with the frozen contrast; Supplementary Section S5). Replacing the cross-year medoid with a direct multi-year median composite changed the contrast negligibly (cosine 0.999 for both indices; Supplementary Section S5), and recompositing with the early-period minimum threshold applied at composite time (five valid observations) reproduced the frozen result (cosine ≥ 0.999; Supplementary Section S2). A pooled July–

August window also retained the three-band structure (cosine 0.995 and 0.994; all 63 bins; Supplementary Section S6); annual-scale July–August analysis is not supported by the early-period archive (median 6.0 valid observations, and fewer than three scenes in six of ten years), so the window check is necessarily pooled.

The cross-sensor check showed that the estimated sensor contrast cannot account for the reorganization (Figure 11). The projection fraction of the estimated sensor contrast onto the observed early-to-recent contrast was 0.249 (95% interval 0.168–0.325) for NDVI and 0.058 (−0.026 to 0.139) for EVI2, and the sensor-adjusted contrast retained the observed structure (cosine similarity 0.877 [0.823–0.908] and 0.900 [0.857–0.934], respectively). Sensor-related differences alone therefore do not explain the southern profile reorganization, although this does not imply that sensor effects are exactly zero: for NDVI, up to about one quarter of the observed contrast (95% interval up to one third) is aligned with the estimated sensor direction, so the check excludes a complete sensor account but not a partial contribution of that size. The bridge design also does not cover the TM-only years before 1999 or OLI-2 acquisitions (2021–2024); both involve same-design sensor pairs with small documented Collection 2 offsets, but they remain unexamined segments of the chain.

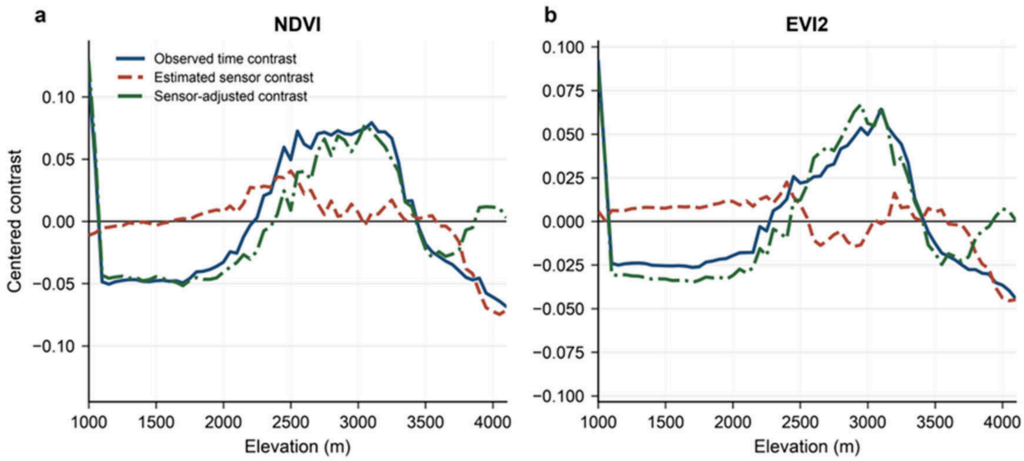


Figure 11. Cross-sensor check of the southern profile contrast (primary design). (**a**) NDVI and (**b**) EVI2: observed early-to-recent contrast (solid), the sensor contrast estimated from overlapping TM–ETM+ and ETM+–OLI bridge periods (dashed), and the sensor-adjusted contrast (dash-dotted). Adjusted contrasts retain the observed structure (cosine similarity 0.877 and 0.900).

3.6. No Directional Consistency with Decadal Hydroclimate Contrasts

Under the separately frozen decadal design, none of the three ERA5-Land variable groups was directionally consistent with the southern vegetation contrast; each was classified as no decadal association (Figure 12), and the same classification held across all six temporal-window × corridor-width scenarios. For temperature (energy), the signed inner product was indistinguishable from zero (NDVI: IP = 0.303, 95% interval −2.52 to 3.44, $p = 0.466$; EVI2: −0.285, −1.97 to 1.55, $p = 0.562$). For soil moisture (the water variable group), the inner product was significantly negative (NDVI: −0.618, −0.97 to −0.32; EVI2: −0.262, −0.45 to −0.10), i.e., the moisture contrast ran opposite to the vegetation contrast; under the frozen one-sided criterion, this is likewise recorded as no association. For snow, the inner product was negative but compatible with zero (NDVI: −0.089, −0.19 to 0.01; EVI2: −0.037, −0.11 to 0.02).

The independent moisture proxy disagreed with the ERA5-Land soil-moisture result. CHIRPS precipitation contrasts were significantly positive (May–August NDVI IP = 538.7, 376.8–730.6; November–May IP = 313.5, 238.1–394.3; both $p < 0.001$). The two moisture proxies therefore point in opposite directions, and neither can be preferred within this

design, so no robust moisture-direction inference is possible. Exploratory northern analyses (uncentered, no gate) showed strong positive energy and snow associations ($\rho \approx 0.82$–0.87, $p = 0.0002$) and negative water associations; these are given without a decision label and, being uncentered, are not comparable in kind with the centered southern test. In sum, under the present decadal, elevation-resolved design, no robust directional correspondence between the confirmed southern reorganization and decadal hydroclimate contrasts was detected; because $D_{veg(z)}$ is mean-centered, this absence of detected correspondence does not rule out approximately uniform hydroclimate forcing and is not evidence that hydroclimate is irrelevant.

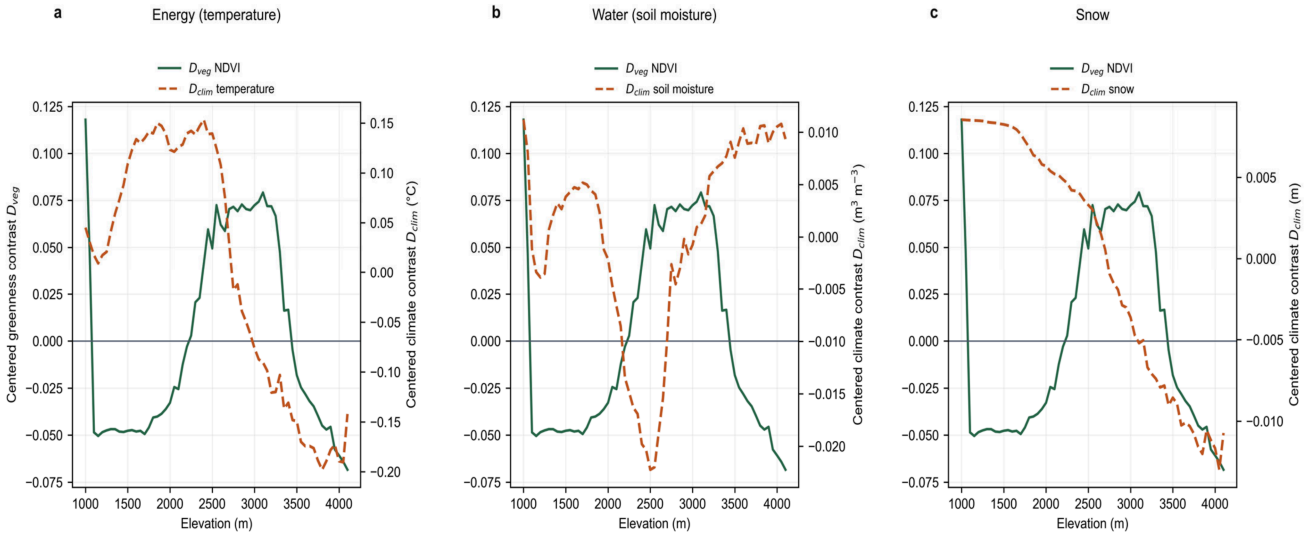


Figure 12. Elevation profiles of the vegetation and decadal climate contrasts in the primary scenario (10 yr, 20 km). Centered NDVI contrast $D_{veg(z)}$ (left axes) overlaid with the centered decadal climate contrast $D_{clim(z)}$ (right axes) for (**a**) near-surface air temperature, (**b**) volumetric soil water, and (**c**) snow water equivalent; the EVI2 overlays are shown in Figure S1.

4. Discussion

4.1. An Elevation-Dependent Redistribution, Not a Simple Hydroclimatic Response

The southern corridor underwent a robust reorganization of the elevation profile of vegetation greenness between the early and recent Landsat periods. In absolute terms, greenness increased almost everywhere, but the increase was four to five times stronger in the mid-elevation band than in the lower and upper bands; in relative terms, this differential amplification reorganized the shape of the whole profile. The negative centered contrasts in the lower and upper bands are therefore relative declines against the profile mean, not absolute browning: absolute greenness increased in all three bands (Section 3.3). Elevation-amplified greening of this kind has been reported in other high-mountain systems, including stronger NDVI trends at mid-to-high elevations in the Himalaya and across Central Asian ranges [42,43], against the broader background of elevation-dependent warming in mountain regions [44], and it is consistent with the broader Tianshan evidence that vegetation change is heterogeneous among belts, subregions, and elevations rather than following a single range-wide pattern [19,20,24]. Our result is also compatible with the post-1998 browning reversal reported for parts of the range [20]. That study describes a reversal in trend direction over time at the regional scale, whereas our comparison contrasts two decadal window means on one flank, so net early-to-recent greening does not contradict mid-period browning.

At the same time, the confirmed contrast was not directionally consistent with decadal temperature, soil-moisture, or snow contrasts, and the two moisture proxies disagreed with

each other (Section 3.6). The reorganization therefore cannot be read as a simple response to decadal hydroclimate means. This absence of directional-consistency parallels the mismatch between greenness and temperature isolines reported for the Tibetan Plateau [3,4] and extends that caution from trend direction to whole-profile shape. Several non-exclusive readings remain open, including responses lagged or nonlinear relative to decadal mean states, controls not represented in the tested variables (such as growing-season snow dynamics, grazing, or land-use change), and scale mismatches between elevation-bin climate aggregates and the processes that structure mountain vegetation. Distinguishing among these requires data and designs beyond the present study; the appropriate conclusion at this stage is that the reorganization is real and elevation-dependent, and that no robust directional correspondence with decadal hydroclimate contrasts was detected under the present decadal, elevation-resolved design—an absence of detected correspondence, not evidence that hydroclimate is irrelevant.

The significantly negative soil-moisture inner product (Section 3.6) likewise deserves discussion rather than being read as a null result. One reading is ecological: the mid-elevation band, where the greenness gain was strongest, may have experienced aggravated water stress as the amplified canopy raised transpiration demand, so that the decadal soil-water contrast ran opposite to the vegetation contrast. A competing, methodological reading is scale mismatch: ERA5-Land cells (~0.1°) smooth the elevation structure analyzed here and resolve neither irrigation withdrawals in the foreland oasis nor snowmelt contributions to root-zone moisture, both of which matter on this flank. That the independent CHIRPS precipitation contrasts point in the opposite direction (Section 3.6) further shows that moisture-direction inference is sensitive to dataset choice. We therefore retain the frozen directional-consistency classification, while noting the negative soil-moisture association as a hypothesis-generating signal for the mechanism-oriented work outlined below.

4.2. Profile Shape Versus Boundary Displacement on This Transect

The profile-level claim stands in instructive contrast to what a boundary-style analysis of the same imagery would have produced. In an exploratory stage of this project, spline-derivative transition candidates on the southern corridor suggested a widening of a T2–T3 functional belt under the primary ten-year design. That candidate failed its prespecified confirmation chain on two independent grounds. Under six-year windows, the T3 candidate was not comparable across indices, with NDVI–EVI2 peak separations of 120–150 m exceeding the 100 m tolerance in all three periods, and an independent BIC-selected segmented-regression estimator reproduced none of the 24 period-specific reference boundary positions. A boundary-based report would thus have presented a displacement that the data could not support under multi-method, multi-window scrutiny.

This experience is directly relevant to how elevational vegetation change is detected. Boundary estimates are statistical constructs whose apparent movement can reflect estimator choice and observation support rather than ecological displacement [14,15], and treeline research has independently moved toward multidimensional ecotone descriptions for related reasons [18]. Our result does not contradict boundary-based findings elsewhere, including the upslope migration of southern Tianshan forest-belt limits reported by Zheng et al. [45]; it shows that, on this transect and under this confirmation standard, the defensible object is the whole-profile reorganization, not the movement of any single derivative-defined boundary. Studies reporting boundary displacement from long-term satellite records would benefit from analogous confirmation chains before interpreting displacement magnitudes.

4.3. Implications of the Spatial and Terrain Organization

The spatial analyses change how the profile result should be read in three ways. First, pervasiveness rules out a local artifact: because nearly all samples and blocks gained

greenness and reorganization is detectable within individual blocks, the three-band pattern is a corridor-scale property rather than the imprint of a few contributing locations. Second, the strength of terrain organization delimits where explanation must be sought. With about two-thirds of the change predictable from terrain structure alone, the remaining third—and especially the sign-mixed residuals in the Kuqa oasis—marks the space in which local and anthropogenic processes operate; treating such lowland agricultural segments separately is essential in corridor studies that span mountain-to-oasis gradients. Third, the dominance of the position–elevation gradient over slope and aspect, which modulate only the amplitude and peak position of the contrast, supports reading the pattern as an elevational rather than a purely topographic phenomenon.

More generally, the fixed-profile framework used here occupies a useful middle ground between pixel-level change mapping and regional averaging. It preserves the vertical structure of the landscape while remaining compact enough for direct statistical testing, and its controls—spatial matching, mean-centering, cross-specification concordance, and sensor falsification—are transferable to other mountain transects, valley profiles, or slope-aspect contrasts where the question concerns the vertical organization of vegetation change.

4.4. Limitations and Future Directions

Several limitations bound the interpretation. The centered contrast describes relative redistribution, not absolute change; we therefore reported absolute sample-level changes alongside, but the primary inference remains shape-based. The analysis conditions on locations valid in all periods, which controls coverage artifacts but restricts inference to persistently observable locations. Equal elevation-bin weighting answers a question about profile shape, not an area-weighted change estimate. The spatial-block permutation and bootstrap procedures approximate, but do not replace, independent spatial replication, and the permutation null is an observational exchangeability argument. The random-forest analysis describes association with terrain structure; elevation and route chainage are strongly collinear along the corridor and must be read jointly, and no causal or climatic interpretation follows from the model's predictive skill. The inference is an endpoint contrast between two decadal mean states; it cannot by itself distinguish a gradual trend from a step change or from multi-year fluctuation, although the middle period—used only for context—is consistent with a gradual progression (Section 3.1).

The spatial scope of inference deserves equal emphasis. All primary inference comes from two terminal corridors of a single highway transect, and mountain roads preferentially follow valleys, passes, and other particular geomorphic settings; the sampled corridors are therefore geographically constrained by the route rather than designed to represent the flank areally. The southern corridor does span the full 1000–4100 m elevational range with dense, spatially matched sampling, and the terrain-stratified analysis (Section 3.4) shows the three-band structure to be stable across the aspect and slope conditions represented within the corridor. Whether the same structure holds across the entire southern flank—including sectors with different valley orientation, geology, and land-use history—cannot be determined from this design and would require area-wide satellite products or additional transects. Statements in this paper should accordingly be read as characterizing the sampled Dushanzi–Kuqa southern corridor.

Observation-related artifacts require separate scrutiny. Fixed-window compositing cannot separate biomass change from phenological shifts: an earlier, elevation-dependent green-up [24] could alter growing-season median greenness without any biomass change, and such shifts need not be elevation-uniform. The confirmed contrast should therefore be read as a change in the growing-season greenness regime, to which phenological timing and biomass both contribute; the present design does not separate these com-

ponents. Observation density also increased over time—median valid growing-season counts rose from 13.6 in the early to 96.3 in the recent period, and 28% of early upper-band samples rest on fewer than five valid observations—so the two periods sample the growing season unevenly; annual-median compositing with the cross-year medoid rule mitigates, but does not eliminate, this asymmetry, although two new checks bound its effect: a density-matched recompositing of the recent period at the early-period observation density retains the three-band structure (Supplementary Section S5), and a pooled July–August window retains it as well (cosine 0.995 and 0.994 with the frozen contrast; Supplementary Section S6), so the pattern is not strongly shaped by seasonal timing within the June–September window; an annual-scale July–August analysis is not supported by the early-period archive (Supplementary Section S6) [28]. Snow persistence is a related high-elevation concern, because snow- and water-flagged observations were retained in the composites (Section 2.2) and snow cover has likely declined between periods: since snow-covered surfaces have low NDVI and EVI2, declining snow persistence would bias recent high-elevation–greenness upward, so the modest absolute increase in the upper band may be overestimated rather than underestimated. The same bias acts against the paper's central pattern, however: inflating recent upper-elevation–greenness can only shrink the mid-elevation-versus-upper-band difference, so the three-band structure is conservative with respect to this artifact. A direct sensitivity check supports this reading: excluding every sample pair with snow-indicating NDSI (>0.4) in either period—1.4% of pairs, concentrated in the upper band, where flagged fractions are similar across periods (11.6% early versus 11.2% recent)—left the statistic, significance, and three-band structure essentially unchanged (NDVI T_{L2} = 2.89 versus 2.92 frozen, p = 0.0002, cosine 0.999 with the frozen contrast). Terrain-illumination effects were not explicitly corrected, but NDVI and EVI2 differ in their illumination sensitivity and produced the same structure, and the aspect-stratified analysis (Section 3.4) found it stable. The 36 specification combinations are also nested rather than independent—they share the same underlying imagery—so the intersection rule protects against isolated positive specifications, not against systematic causes common to all combinations; the artifact-specific checks above carry that burden.

The decadal hydroclimate test evaluates directional consistency of decadal means only; it does not test interannual, lagged, or process-specific mechanisms, it has no power against climate contrasts that are uniform across elevation (Section 2.7), and the disagreement between the ERA5-Land soil-moisture and CHIRPS precipitation proxies indicates that moisture-direction inference is sensitive to dataset choice. No field survey or historical vegetation map is available to interpret the reorganization semantically; the northern corridor did not pass the full confirmation rule and was used only for context, and the central high-mountain section of the transect remains unanalyzed.

Three directions follow directly. A test of hydroclimate association at interannual or lagged scales would require a new, independently specified temporal design rather than a relaxation of the present decadal gate. Mechanism-oriented work should bring in independent constraints—grazing and land-use records, snow-duration products, and vegetation-composition data—so that the open readings in Section 4.1 can be distinguished. Finally, semantic validation of the contributing elevation bands, for example through high-resolution imagery time series or targeted field sampling, would connect the profile-scale signal to vegetation processes on the ground.

5. Conclusions

This study treated the elevation profile of vegetation greenness itself as the analytical object and asked whether its shape reorganized between 1989 and 2024 along the Dushanzi–Kuqa transect on the southern flank of the Chinese Tianshan. It did: relative to the profile mean, green-

ness declined at 1100–1950 m and 3550–4100 m while increasing at 2550–3300 m—a three-band structure that held for both NDVI and EVI2, passed an intersection rule across 36 specification combinations, and survived cross-sensor falsification. Because absolute greenness increased across nearly the entire corridor (97.7% of 25,334 samples), these declines are relative redistributions against the profile mean, not vegetation loss: the profile was reorganized by a roughly four-to-five-fold differential amplification of an otherwise pervasive increase.

Two implications follow for mountain vegetation monitoring. First, profile shape captures a mode of change that mean trends and boundary-displacement metrics can both miss, and the two should not be conflated: a boundary-style analysis of the same imagery failed a prespecified confirmation chain, illustrating how estimator-dependent displacement claims can diverge from what the data support. Second, the spatial analyses delimit where explanation must be sought. With about two-thirds of the change predictable from terrain structure under out-of-sample evaluation and sign-mixed residuals confined to the Kuqa oasis, lowland agricultural segments must be treated separately from the mountain signal in corridor studies that span mountain-to-oasis gradients.

The scope and interpretation of the results should be kept within the design. All inference comes from the sampled Dushanzi–Kuqa southern corridor and does not by itself establish range-wide patterns; the negative centered contrasts describe relative redistribution, not browning; and under the present decadal, elevation-resolved design no robust directional correspondence with decadal temperature, soil-moisture, or snow contrasts was detected—an absence of detected correspondence rather than evidence that hydroclimate plays no role. Explaining the reorganization will require independent constraints on land use, snow dynamics, and vegetation composition. Treating the elevational greenness profile as the analytical object—with spatially matched sampling, mean-centering, and cross-specification confirmation—provides a transferable way to detect mountain vegetation redistribution without misreading it as boundary migration or as a simple climate response.

Supplementary Materials: The following supporting information can be downloaded at: https://www.mdpi.com/article/10.3390/rs18213734/s1, Figure S1: EVI2 counterparts of the NDVI-based main-text figures. (a) Observed ΔEVI2 over the southern corridor (counterpart of Figure 7a); (b) stratified centered EVI2 contrasts across aspect and slope strata (counterpart of Figure 9); (c) three-period mean-centered EVI2 profiles and (d) early-to-middle and early-to-recent centered EVI2 contrasts (counterparts of Figure 6a,b; Pearson r = 0.97, 63 bins); (e)–(g) decadal climate overlays of the centered EVI2 contrast against near-surface air temperature, volumetric soil water, and snow water equivalent (counterparts of Figure 12a–c). Table S1: Early-period minimum-observation threshold sensitivity of the frozen primary test (south, 10-year windows, 20 km corridor, 50 m bins; 4999 block-level permutations). Figure S2: Centered contrasts D(z) of the frozen primary design (dashed) and of reruns excluding early-period sample pairs with fewer than 5, 8, or 10 valid observations. (a, b) NDVI and EVI2 contrasts; (c, d) difference from the frozen contrast. The three-band structure and the upper-band relative decline are retained at all thresholds; curves truncate where bins lose support at t = 8 and t = 10. Table S2: Multi-index replication of the frozen south-slope test (63 × 50 m bins; 4999 block-level permutations). SAVI and MSAVI were evaluated on the WorldCover-defined support subset (62 of 63 bins; Section S7); Figure S3: Centered contrasts D(z) for the frozen NDVI and EVI2 analyses and for the two added indices (kNDVI, NDMI) on the same matched samples. (a) Original index scales; (b) contrasts normalized by their own standard deviation for shape comparison. All four indices reproduce the three-band structure with $p < 0.001$. Table S3: Collinearity-aware permutation importance of the terrain random forest (drop in held-out R^2; after permutation; mean ± SD over 50 scores = 10 spatial-block folds × 5 repeats). Top: joint and single-variable permutation. Bottom: conditional permutation within five quantile strata of the other predictor. Figure S4: Collinearity-aware random-forest importance. (a) Joint versus single-variable permutation importance for the

elevation–chainage pair and the remaining terrain attributes. (b) Conditional permutation importance within quantile strata of the other predictor. Error bars are SD over 50 scores. Elevation retains most of its importance within chainage strata, whereas chainage retains little within elevation strata. Table S4: Compositing-rule and density-matched reruns of the frozen primary test (south, 10-year windows, 20 km corridor, 50 m bins; 4999 block-level permutations). Figure S5: Centered contrasts D(z) for (a) the multi-year median composite and (b) the density-matched recent recompositing, each with the frozen contrast (dashed). Both variants retain the three-band structure ($p < 0.001$). Table S5: Pooled July–August window rerun of the frozen primary test and the associated coverage audit. Figure S6: (a) Centered contrasts D(z) for the pooled July–August window versus the frozen contrast (dashed). (b) Early-period median valid observation counts under the June–September and July–August windows by elevation band, with sample retention annotated. Table S6: Cropland-exclusion rerun of the frozen primary test (south, 10-year windows, 20 km corridor, 50 m bins; 4999 block-level permutations). Figure S7: (a) Centered contrasts D(z) before and after excluding cropland-labeled samples (ESA WorldCover 2021). (b) Cropland share of lower-band contrast energy by index; cropland makes up 0.97% of lower-band samples.

Author Contributions: Conceptualization, Z.D., X.K. and Y.M.; methodology, Z.D., X.K. and Y.M.; software, Z.D., X.K. and Z.W.; validation, Z.D.; formal analysis, Z.D.; investigation, Z.D. and Y.M.; resources, Z.D. and Y.M.; data curation, Z.D. and M.L.; writing—original draft preparation, Z.D., Y.M., M.L. and W.W.; writing—review and editing, Z.D., Y.M. and M.L.; visualization, L.L. and L.Z.; supervision, Z.D. and Y.M.; project administration, Z.D., Y.M. and M.L. All authors have read and agreed to the published version of the manuscript.

Funding: This research was supported by the Science and Technology Program of Gansu Province (No. 25JRRA535), Science and Technology Program of Gansu Province (No. 23ZDFA017).

Data Availability Statement: The satellite, terrain, and climate datasets used in this study are publicly available from the Google Earth Engine data catalog, including Landsat Collection 2 Level-2 surface reflectance products. Copernicus DEM GLO-30, ERA5-Land monthly aggregates, CHIRPS precipitation data, and OpenStreetMap data were used to delineate the highway centerline. Derived analysis code and processed tabular outputs are available from the authors upon reasonable request.

Conflicts of Interest: The authors declare no conflicts of interest.

References

1. Körner, C. The use of 'altitude' in ecological research. *Trends Ecol. Evol.* **2007**, *22*, 569–574. [CrossRef]
2. Rumpf, S.B.; Hülber, K.; Klonner, G.; Moser, D.; Schütz, M.; Wessely, J.; Willner, W.; Zimmermann, N.E.; Dullinger, S. Range dynamics of mountain plants decrease with elevation. *Proc. Natl. Acad. Sci. USA* **2018**, *115*, 1848–1853. [CrossRef]
3. An, S.; Zhu, X.; Shen, M.; Wang, Y.; Cao, R.; Chen, X.; Yang, W.; Chen, J.; Tang, Y. Mismatch in elevational shifts between satellite observed vegetation greenness and temperature isolines during 2000-2016 on the Tibetan Plateau. *Glob. Change Biol.* **2018**, *24*, 5411–5425. [CrossRef]
4. Zhang, L.; Shen, M.; Yang, Z.; Wang, Y.; Chen, J. Spatial variations in the difference in elevational shifts between greenness and temperature isolines across the Tibetan Plateau grasslands under warming. *Sci. Total Environ.* **2024**, *906*, 167715. [CrossRef]
5. Anderson, K.; Fawcett, D.; Cugulliere, A.; Benford, S.; Jones, D.; Leng, R. Vegetation expansion in the subnival Hindu Kush Himalaya. *Glob. Change Biol.* **2020**, *26*, 1608–1625. [CrossRef]
6. Leng, R.; Harrison, S.; Fawcett, D.; Tiwari, A.; Harrison, M.; Anderson, K. Vegetation on the move: Elevational shifts and greening dynamics across the Himalayan alpine zone. *Ecography* **2026**, *2026*, e08259. [CrossRef]
7. Mukhtar, H.; Yang, Y.; Xu, M.; Wu, J.; Abbas, S.; Wei, D.; Zhao, W. Elevation-dependent vegetation greening and its responses to climate changes in the south slope of the Himalayas. *Geophys. Res. Lett.* **2025**, *52*, e2024GL113276. [CrossRef]
8. Macek, M.; Prošek, J.; Doležal, J.; Wild, J.; Ježek, V.; Kopecký, M. Elevation-dependent sensitivity of spectral greening to temperature and precipitation in the Western Himalayas. *Environ. Res. Lett.* **2025**, *20*, 054078. [CrossRef]
9. Rumpf, S.B.; Gravey, M.; Brönnimann, O.; Luoto, M.; Cianfrani, C.; Mariethoz, G.; Guisan, A. From white to green: Snow cover loss and increased vegetation productivity in the European Alps. *Science* **2022**, *376*, 1119–1122. [CrossRef]
10. Fadrique, B.; Báez, S.; Duque, Á.; Malizia, A.; Blundo, C.; Carilla, J.; Osinaga-Acosta, O.; Malizia, L.; Silman, M.; Farfán-Ríos, W.; et al. Widespread but heterogeneous responses of Andean forests to climate change. *Nature* **2018**, *564*, 207–212. [CrossRef]

11. Tai, X.; Epstein, H.E.; Li, B. Elevation and climate effects on vegetation greenness in an arid mountain-basin system of Central Asia. *Remote Sens.* **2020**, *12*, 1665. [CrossRef]
12. Pan, N.; Feng, X.; Fu, B.; Wang, S.; Ji, F.; Pan, S. Increasing global vegetation browning hidden in overall vegetation greening: Insights from time-varying trends. *Remote Sens. Environ.* **2018**, *214*, 59–72. [CrossRef]
13. de Klerk, H.M.; Burgess, N.D.; Visser, V. Probabilistic description of vegetation ecotones using remote sensing. *Ecol. Inform.* **2018**, *46*, 125–132. [CrossRef]
14. Fortin, M.-J.; Olson, R.J.; Ferson, S.; Iverson, L.; Hunsaker, C.; Edwards, G.; Levine, D.; Butera, K.; Klemas, V. Issues related to the detection of boundaries. *Landsc. Ecol.* **2000**, *15*, 453–466. [CrossRef]
15. Fagan, W.F.; Fortin, M.-J.; Soykan, C. Integrating edge detection and dynamic modeling in quantitative analyses of ecological boundaries. *BioScience* **2003**, *53*, 730–738. [CrossRef]
16. Montesano, P.M.; Neigh, C.S.R.; Sexton, J.; Feng, M.; Channan, S.; Ranson, K.J.; Townshend, J.R. Calibration and validation of Landsat tree cover in the taiga-tundra ecotone. *Remote Sens.* **2016**, *8*, 551. [CrossRef]
17. Wan, H.; Guo, P.; Luo, L.; Zhao, Y.; Zhao, Y.; Wang, X. Different remote sensing indicators reveal the transitions of two states along elevation gradients within the Xinjiang Tianshan Bogda Natural World Heritage Site. *Int. J. Appl. Earth Obs. Geoinf.* **2022**, *111*, 102842. [CrossRef]
18. Garbarino, M.; Morresi, D.; Anselmetto, N.; Weisberg, P.J. Treeline remote sensing: From tracking treeline shifts to multi-dimensional monitoring of ecotonal change. *Remote Sens. Ecol. Conserv.* **2023**, *9*, 729–742. [CrossRef]
19. Zhang, Y.; Liu, L.-Y.; Liu, Y.; Zhang, M.; An, C.-B. Response of altitudinal vegetation belts of the Tianshan Mountains in northwestern China to climate change during 1989-2015. *Sci. Rep.* **2021**, *11*, 4870. [CrossRef]
20. Li, Y.; Chen, Y.; Sun, F.; Li, Z. Recent vegetation browning and its drivers on Tianshan Mountain, Central Asia. *Ecol. Indic.* **2021**, *129*, 107912. [CrossRef]
21. Jiao, W.; Wang, L.; Smith, W.K.; Chang, Q.; Wang, H.; D'Odorico, P. Observed increasing water constraint on vegetation growth over the last three decades. *Nat. Commun.* **2021**, *12*, 3777. [CrossRef]
22. Su, Y.; Chen, S.; Li, X.; Ma, S.; Xie, T.; Wang, J.; Yan, D.; Chen, J.; Feng, M.; Chen, F. Changes in vegetation greenness and its response to precipitation seasonality in Central Asia from 1982 to 2022. *Environ. Res. Lett.* **2023**, *18*, 104002. [CrossRef]
23. Pei, H.; Li, G.; Wang, Y.; Peng, J.; Li, M.; Yao, J.; Wei, T. Trend shifts in vegetation greening and responses to drought in Central Asia, 1982–2022. *Forests* **2025**, *16*, 1575. [CrossRef]
24. Ding, C.; Huang, W.; Liu, M.; Zhao, S. Change in the elevational pattern of vegetation greenup date across the Tianshan Mountains in Central Asia during 2001-2020. *Ecol. Indic.* **2022**, *136*, 108684. [CrossRef]
25. Wulder, M.A.; Masek, J.G.; Cohen, W.B.; Loveland, T.R.; Woodcock, C.E. Opening the archive: How free data has enabled the science and monitoring promise of Landsat. *Remote Sens. Environ.* **2012**, *122*, 2–10. [CrossRef]
26. Zhu, Z. Change detection using Landsat time series: A review of frequencies, preprocessing, algorithms, and applications. *ISPRS J. Photogramm. Remote Sens.* **2017**, *130*, 370–384. [CrossRef]
27. Qiu, S.; He, B.; Zhu, Z.; Liao, Z.; Quan, X. Improving Fmask cloud and cloud shadow detection in mountainous area for Landsats 4-8 images. *Remote Sens. Environ.* **2017**, *199*, 107–119. [CrossRef]
28. Bayle, A.; Gascoin, S.; Berner, L.T.; Choler, P. Landsat-based greening trends in alpine ecosystems are inflated by multidecadal increases in summer observations. *Ecography* **2024**, *2024*, e07394. [CrossRef]
29. Cohen, W.B.; Healey, S.P.; Yang, Z.; Stehman, S.V.; Brewer, C.K.; Brooks, E.B.; Gorelick, N.; Huang, C.; Hughes, M.J.; Kennedy, R.E.; et al. How similar are forest disturbance maps derived from different Landsat time series algorithms? *Forests* **2017**, *8*, 98. [CrossRef]
30. Zeng, Y.; Hao, D.; Park, T.; Zhu, P.; Huete, A.; Myneni, R.; Knyazikhin, Y.; Qi, J.; Nemani, R.R.; Li, F.; et al. Structural complexity biases vegetation greenness measures. *Nat. Ecol. Evol.* **2023**, *7*, 1790–1798. [CrossRef]
31. Huete, A.R. A soil-adjusted vegetation index (SAVI). *Remote Sens. Environ.* **1988**, *25*, 295–309. [CrossRef]
32. Qi, J.; Chehbouni, A.; Huete, A.R.; Kerr, Y.H.; Sorooshian, S. A modified soil adjusted vegetation index. *Remote Sens. Environ.* **1994**, *48*, 119–126. [CrossRef]
33. Camps-Valls, G.; Campos-Taberner, M.; Moreno-Martínez, Á.; Walther, S.; Duveiller, G.; Cescatti, A.; Mahecha, M.D.; Muñoz-Marí, J.; García-Haro, F.J.; Guanter, L.; et al. A unified vegetation index for quantifying the terrestrial biosphere. *Sci. Adv.* **2021**, *7*, eabc7447. [CrossRef]
34. Badgley, G.; Field, C.B.; Berry, J.A. Canopy near-infrared reflectance and terrestrial photosynthesis. *Sci. Adv.* **2017**, *3*, e1602244. [CrossRef]
35. U.S. Geological Survey. *Landsat 4-7 and Landsat 8-9 Collection 2 Level-2 Science Product Guides*; U.S. Geological Survey: Reston, VA, USA, 2024.
36. Rouse, J.W.; Haas, R.H.; Schell, J.A.; Deering, D.W. Monitoring vegetation systems in the Great Plains with ERTS. In Proceedings of the Third Earth Resources Technology Satellite-1 Symposium, Washington, DC, USA, 10–14 December 1974; pp. 309–317.

37. Jiang, Z.; Huete, A.R.; Didan, K.; Miura, T. Development of a two-band enhanced vegetation index without a blue band. *Remote Sens. Environ.* **2008**, *112*, 3833–3845. [CrossRef]
38. Gao, B.-C. NDWI—A normalized difference water index for remote sensing of vegetation liquid water from space. *Remote Sens. Environ.* **1996**, *58*, 257–266. [CrossRef]
39. European Space Agency. Copernicus Global Digital Elevation Model. Distributed by OpenTopography. 2024. Available online: https://portal.opentopography.org/datasetMetadata?otCollectionID=OT.032021.4326.1 (accessed on 23 July 2026).
40. Zanaga, D.; Van De Kerchove, R.; Daems, D.; De Keersmaecker, W.; Brockmann, C.; Kirches, G.; Wevers, J.; Cartus, O.; Santoro, M.; Fritz, S.; et al. ESA WorldCover 10 m 2021 v200. *Zenodo*. 2022. Available online: https://zenodo.org/records/7254221 (accessed on 15 August 2026).
41. Yang, J.; Huang, X. The 30 m annual land cover dataset and its dynamics in China from 1990 to 2019. *Earth Syst. Sci. Data* **2021**, *13*, 3907–3925. [CrossRef]
42. Nila, M.U.S.; Bobrowski, M.; Schickhoff, U. Growing season normalized difference vegetation index in the Nepal Himalaya and adjacent areas, 2000–2019: Sensitivity to climate change and terrain factors. *Land* **2025**, *14*, 749. [CrossRef]
43. Li, M.; Yao, J.; Zheng, J. Spatio-temporal change and drivers of the vegetation trends in Central Asia. *Forests* **2024**, *15*, 1416. [CrossRef]
44. Pepin, N.; Bradley, R.S.; Diaz, H.F.; Baraer, M.; Caceres, E.B.; Forsythe, N.; Fowler, H.; Greenwood, G.; Hashmi, M.Z.; Liu, X.D.; et al. Elevation-dependent warming in mountain regions of the world. *Nat. Clim. Change* **2015**, *5*, 424–430. [CrossRef]
45. Zheng, L.; Zhang, Y.; Lu, C.; Zhang, W.; Tan, B.; Jiang, L.; Zhang, Y.; An, C. Response of forest belt on the south slope of Tianshan Mountains in China to global warming during 1990-2020. *Front. Earth Sci.* **2024**, *18*, 831–848. [CrossRef]

Disclaimer/Publisher's Note: The statements, opinions and data contained in all publications are solely those of the individual author(s) and contributor(s) and not of MDPI and/or the editor(s). MDPI and/or the editor(s) disclaim responsibility for any injury to people or property resulting from any ideas, methods, instructions or products referred to in the content.